Analysis of converted-wave extended images for migration velocity analysis

Jia Yan & Paul Sava

ABSTRACT

Converted-wave data have been recognized to have potential in complementing conventional compressional data. However, imaging for converted-waves is more difficult mainly due to the need for estimating shear-wave velocities, in addition to compressional-wave velocities. The common practice is to obtain the shear-wave velocity by registering PS and PP images. Despite its low cost, this procedure is prone to error due to the assumption of imaging simple structure and due to the high potential for cycle skipping. On the other hand, we could obtain S velocities by adapting wave-equation migration velocity analysis (MVA) tools for shear waves. Our assumption is that we can update the S velocities while keeping the known P velocity fixed. We assume that the P-wave velocity is known from MVA of the PP component of the data, then we estimate the S-wave velocity from MVA on the PS component of the data. If P- and S-wave velocities are all correctly estimated, corresponding PP and PS events match in the migrated depth sections. This velocity analysis can make use of both common image gathers (CIGs) and common image point gathers (CIPs). We derive the moveout function for CIPs of converted-wave images and find that they present more complicated moveout than their pure-mode counterparts. We explore the applicability of differential semblance optimization (DSO) to the PP and PS gathers (CIPs and CIGs) to obtain objective functions, based which we can construct optimal velocity models. We find that the objective functions for both PP and PS data are convex, which warrants their use for migration velocity analysis using efficient gradient-descent numerical optimization schemes.

Key words: velocity analysis, common image point gathers, coverted-waves

1 INTRODUCTION

Multicomponent data are acquired both on land and at ocean bottom because converted-waves have been recognized to have potential advantages in several aspects. Converted waves can produce better images of the Earth structure where P-waves have small reflectivity and S-waves have larger reflectivity. Converted waves also complement P-waves in imaging through zones where P-waves are highly attenuated and S-waves are less affected, e.g., gas-concentrated area. Converted-waves also provide invaluable information for lithology estimations, anisotropy parameter estimations, and reservoir characterization (Stewart et al., 2002, 2003).

Despite its usefulness, imaging with converted-waves has not gained the same popularity as imaging with acoustic waves for the following reasons. First, it is much more expensive to acquire multicomponent data than single-component data. Second, it is more difficult to pre-process converted-wave data. For example, gathering, mapping, and binning for converted-wave data are more complicated than pure-mode data due to the asymmetry of PS wave raypaths (Stewart et al., 2002; Thomsen, 1998). Third, it is more difficult to image with converted-wave data because both P- and S-wave velocities are needed. Furthermore, because of the strong influence of anisotropy on shear-waves, the isotropy assumption which cause less problems to acoustic-wave imaging is often insufficient for converted-wave data. This makes it necessary to estimate for additional model parameters, which is theoretically and computationally challenging.

Many authors, including Nicoletis et al. (1998); Kendall et al. (1998); Dai et al. (2000), investigate methods for time or depth migration using converted-wave data. The migration procedures for PP and PS data do not differ in nature, and both include two basic steps: the reconstruction of source

and receiver wavefields at all locations in the subsurface and the application of an imaging condition to extract reflectivity from the reconstructed wavefields. The main difference is that for PP data, both source and receiver wavefields are reconstructed using P-wave velocity; for PS data, source and receiver wavefields are reconstructed with P- and S-wave velocities, respectively. Herrenschmidt et al. (2001) compare various approaches for obtaining migration velocities for converted-wave imaging. They find that time migration is acceptable only when the model has little lateral velocity variation, otherwise only positive or negative offsets get flattened. They conclude that imaging PS data with a prestack depth migration approach most naturally handles complexities in the model.

One of the most difficult problems for imaging with converted-waves is to obtain correct migration models. Although it is common knowledge that prestack depth migration generates better images than time migration, the PS migration velocity is still usually obtained in the time domain, mainly due to a lower cost. The velocity estimation for shear-waves is mostly carried out by the so-called "registration" process: shear-wave velocities are estimated or tuned by correlating corresponding PP and PS reflections in the time-migrated seismic sections and stretching in time the PS section to match with the PP section using the estimated V_P/V_S ratio. Initially, the registration process involves manual picking to correlate PP and PS events (Gaiser, 1996). Later, many authors, including Ogiesoba & Stewart (2003), Fomel & Backus (2003), Nickel & Sonneland (2004), Fomel et al. (2005), and Yuan et al. (2008), develop methods to improve the automation and efficiency of the registration process. Since PP and PS data do not have the same frequency contents, usually a spectral-whitening to both components is necessary to match the PP and PS events. The registration technique has the benefit of fast performance because the operation is usually carried out in the time domain and is relatively not time-consuming. However, velocity analysis using image registration has some inherent problems. First, P- and S-waves are assumed to have similar reflectivity in a long-wavelength scale. This assumption is sometimes violated, since PP and PS waves do not necessarily respond equally to all reflectors. Second, the registration process is prone to cycle-skipping without the aid of well logs. Third, the registration process makes the assumption that there is no lateral mispositioning of the PS image (Fomel & Backus, 2003), and therefore all adjustments of shear-wave velocity are local and vertical.

An alternative for obtaining the S-wave velocities is to carry out a joint PP and PS inversion (Veire & Landrø, 2006; Margrave et al., 2001). The joint inversion technique starts with a rough estimate of V_P/V_S ratio to register corresponding PP and PS events and then inverts for the elastic parameters using approximate PP and PS reflection coefficients (amplitude versus offset (AVO) response). The main benefit of the joint inversion is that it not only estimates V_P and V_S, but also the density ρ, which is an important elastic parameter for lithology analysis. The joint inversion technique, however, also requires registering PP and PS events. Moreover, a key problem, as pointed out by Veire & Landrø (2006), is the difficulty in converting PP and PS seismic amplitudes into true reflection coefficients, especially for complex geology. In these situations, a more sophisticated analysis that converts data to true incidence/reflection angles and inverts with AVA (amplitude versus angle) is necessary (Veire & Landrø, 2006).

Most existing shear-wave velocity analysis tools require registration of PP and PS events in order to estimate the V_P/V_S ratio. This is usually difficult when pure- and converted-waves have different frequency contents, are subject to different reflection coefficients, and the wavelets of the two wave modes are inconsistent with each other. In this paper, we explore the possibility of wave-equation MVA in the depth domain for the shear-mode using converted-wave data only, i.e., we update the S velocity after P velocity analysis, while keeping the P velocity fixed. We assume that the velocity of the P-wave is known from MVA of the PP component of the data, and then we perform MVA on the PS component only. This approach is analog to the layer-stripping approach used for velocity model building for simple structures. In the layer-stripping technique, velocity estimates for the deeper layers rely on the velocity estimates for the shallow layers. This procedure, if not done correctly, introduces velocity errors to the deeper layers from errors accumulated in the shallow layers. The MVA procedure which estimates P- and S-wave velocities independently is subject to a similar problem. Although errors in the *a priori* P-wave velocity might be translated into S-wave velocity, this procedure has the benefit that we do not need to register the PS and PP events. If P- and S-wave velocities are all correctly estimated, corresponding PP and PS events should match in the depth migrated sections.

Wavefield tomography iteratively updates the model by minimizing an objective function. The objective function characterizes the data misfit and reaches its minimum when the velocity model is correct. For seismic data, one can invert for the model in the data domain using a technique commonly known as full waveform inversion (FWI) (Tarantola, 1987; Mora, 1988; Song et al., 1995; Pratt & Worthington, 1990; Pratt, 1999), or in the image domain using a technique commonly known as wave-equation migration velocity analysis (WEMVA) (Biondi & Sava, 1999; Shen et al., 2003; Albertin et al., 2006; Yang & Sava, 2009).

The objective function for WEMVA exploits the errors from extended images due to the incorrect migration velocity. Subsets of extended images can be organized as common-image gathers (CIGs) or common-image point gathers (CIPs) (Sava & Vasconcelos, 2010). The CIGs can be computed in different domains, for example, space-lag domain (Rickett & Sava, 2001), time-lag domain (Sava & Fomel, 2006), space- and time-lag domain(Yang & Sava, 2008), and angle domain (Sava & Fomel, 2003; Yan & Sava, 2008). Velocity errors are characterized by the features of the events, for example misfocusing of the events in the space-lag domain, deviation from zero time-lag in the time-lag domain, or non-flatness of the events in the angle-domain.

Sava & Vasconcelos (2010) develop the concept of CIPs and argue that computational cost for construction of CIPs decreases compared to the cost of constructing regular CIGs.

They derive the moveout function of CIP events for pure-mode and suggest their use for migration velocity analysis. In this paper, we derive the moveout of CIPs for converted-waves, discuss their features, and compare the CIPs for pure-mode and converted-mode waves. We find that compared to PP CIPs, the PS CIPs are characterized by more complicated moveout, which increases the difficulty of using them for migration velocity analysis.

We begin this paper with a review of PP and PS CIGs in the space-lag and angle domains and analyze the differences between the gathers obtained with both correct and incorrect migration velocities. We discuss the influence of the polarity reversal, which exist in both the PS data and the corresponding CIGs. Then we formulate DSO type penalty functions (Shen & Symes, 2008) for pure- and converted-mode data and show that the corresponding objective functions are convex functions suitable for numerical optimization with gradient based techniques.

2 COMMON IMAGE GATHERS

In wave-equation migration, images are obtained through two successive steps: the reconstruction of the source and receiver wavefields and the application of an imaging condition. A conventional imaging condition takes the zero-lag cross correlation of the source and receiver wavefields in both space and time to form an image. This imaging condition, however, does not carry velocity error information. An extended imaging condition is formulated as taking non-zero lags in space and time to retrieve the velocity error:

$$R(\mathbf{x},\boldsymbol{\lambda},\tau)=\sum_{\omega}\overline{W_s(\mathbf{x}+\boldsymbol{\lambda},\omega)}\,W_r(\mathbf{x}-\boldsymbol{\lambda},\omega)e^{2i\omega\tau}\,. \quad (1)$$

Here, $\mathbf{x}=\{x,y,z\}$ denotes the image point coordinates, ω is the angular frequency used to extrapolate the the source and receiver wavefield, W_s and W_r. The variables $\boldsymbol{\lambda}$ and τ are the space- and time-lags, respectively. The over-line indicates complex conjugate. The extended imaging condition provides access to information usable for migration velocity analysis.

Since using both space- and time-lags is computationally expensive, it is desirable to work on subsets of the extended images, e.g., space-lag common image gathers, time-lag common image gathers, or space-time-lag common image point gathers. These subsets of the extended images are cheaper to construct because either some of the lags are set to zero or the full lags are computed at a limited number of points distributed throughout the image.

2. 1 Space-lag-domain common image gathers

To construct common image gathers at certain desired image locations, a special case of the extended imaging condition which uses only space-lags $\boldsymbol{\lambda}=\{\lambda_x,\lambda_y,\lambda_z\}$ is often adopted:

$$R(\mathbf{x},\boldsymbol{\lambda})=\sum_{\omega}\overline{W_s(\mathbf{x}+\boldsymbol{\lambda},\omega)}\,W_r(\mathbf{x}-\boldsymbol{\lambda},\omega)\,. \quad (2)$$

This special case of extended images is often used to construct space-lag common image gathers (Rickett & Sava, 2001; Sava & Fomel, 2005a). The space-lag gathers are used for velocity analysis and indicate velocity errors by misfocusing from zero space lags.

2. 2 Angle-domain common image gathers

Angle-domain common image gathers are often constructed for migration velocity analysis (MVA) or amplitude versus angle (AVA) analysis. They can also be used for velocity analysis and indicate velocity errors by unflatness of the events. To obtain an angle-domain CIG, one needs to map the lag-domain CIG constructed by equation 2 to the angle domain. A general equation for the angle decomposition is formulated by Sava & Fomel (2005b):

$$\tan^2\theta=\frac{(1+\gamma)^2\left|\mathbf{k}_{\boldsymbol{\lambda}}\right|^2-(1-\gamma)^2\left|\mathbf{k}_{\mathbf{x}}\right|^2}{(1+\gamma)^2\left|\mathbf{k}_{\mathbf{x}}\right|^2-(1-\gamma)^2\left|\mathbf{k}_{\boldsymbol{\lambda}}\right|^2} \quad (3)$$

where γ is the velocity ratio of the source and receiver wavefields at the CIG location. The variables $\mathbf{k}_{\mathbf{x}}$ and $\mathbf{k}_{\boldsymbol{\lambda}}$ are the wave vectors for the image point coordinates $\mathbf{x}$ and space-lag vector $\boldsymbol{\lambda}$, respectively. The angle θ is half of the opening angle between the source and receiver rays. Angle gathers can be used for MVA by exploiting the fact that reflections are not flat when data are imaged with incorrect velocity.

3 COMMON IMAGE POINT GATHERS

The space-lag common image gathers use only the space lags and set the time lag to zero, thus discarding valuable information which could be used to characterize velocity errors. Therefore, it is desirable to utilize all types of lags to characterize velocity errors. A major implementation problem is that the extended images using all space- and time-lags are seven-dimensional objects, which are too computationally demanding and require large storage. To reduce the storage and computational cost, Sava & Vasconcelos (2010) introduce the concept of common-image-point gathers (CIPs), which are simply subsets of the extended images constructed at sparse locations in the subsurface. The construction of the CIPs allows us to extend the images to all space and time lags, while reducing the overall computation cost compared to regular CIGs.

In this section, we derive the moveout equation for common image point (CIP) gathers for converted-waves, assuming imaging with both a single shot and multiple shots. The moveout functions offer insight into the expected behavior of such CIPs in areas of complex velocity variations (Sava & Vasconcelos, 2010) and form the basis for the definition of an objective function used for migration velocity analysis.

3. 1 CIP moveout for imaging with a single shot

We use Figure 1 to illustrate the notations adopted in our derivation. In this schematic, the vector $\mathbf{q}$ denotes the direction along which the reflector and the reflection plane inter-

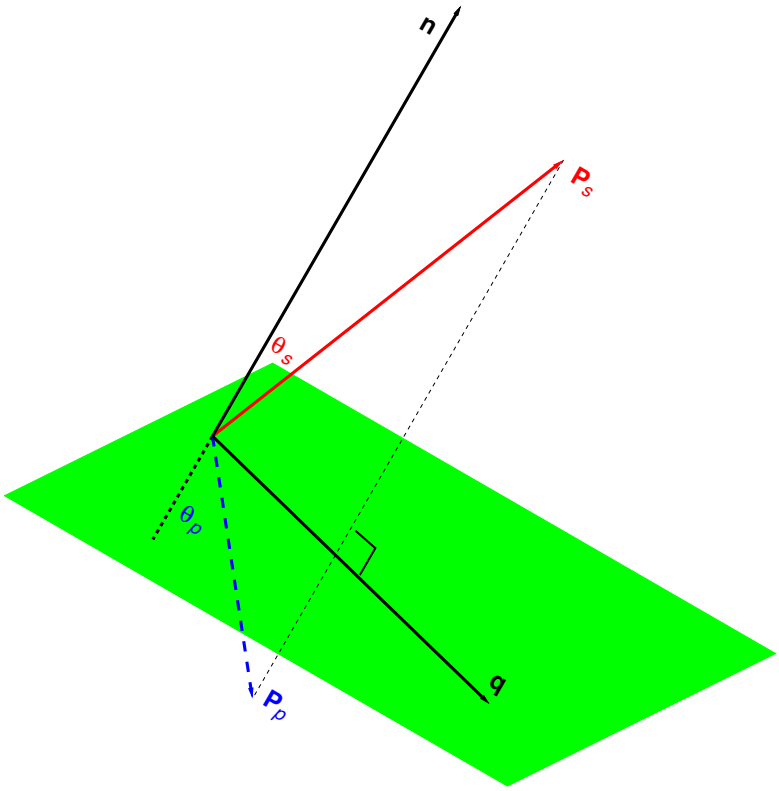


Figure 1. Schematic illustrating a P to S reflection upon a reflector. The reflection plane and the reflector intersect a line defined by the vector $\mathbf{q}$. The reflector has a normal defined by the vector $\mathbf{n}$. The source and receiver rays are characterized by the vectors $\mathbf{p}_p$ and $\mathbf{p}_s$, respectively. The incidence and reflection angles are denoted by θ_p and θ_s, respectively.

sect, and the vector $\mathbf{n}$ denotes the reflector normal. For a P-wave ray vector $\mathbf{p}_p$ incident upon the reflector at an angle θ_p, the S-wave ray $\mathbf{p}_s$ is reflected at an angle θ_s. The incidence and reflection angles are related by the Snell's law:

$$\frac{\sin\theta_p}{v_p} = \frac{\sin\theta_s}{v_s}\,, \tag{4}$$

where v_p and v_s are the P- and S-wave velocities, respectively. The Snell's law simply states that the slowness along the reflector is preserved regardless of the reflector dip. We can express the source and receiver ray vectors as:

$$\mathbf{p}_p = \frac{\mathbf{n}_p}{v_p}\,, \tag{5}$$

$$\mathbf{p}_s = \frac{\mathbf{n}_s}{v_s}\,, \tag{6}$$

where $\mathbf{n}_p$ and $\mathbf{n}_s$ are unit vectors along the source and receiver rays, respectively.

We begin with the conventional imaging condition for P to S reflection. For a subsurface image point $\mathbf{x}$, the conventional imaging condition can be expressed as the intersection of two planes given by the expressions

$$\mathbf{p}_p \cdot \mathbf{x} \;=\; 0\,, \tag{7}$$

$$\mathbf{p}_s \cdot \mathbf{x} \;=\; 0\,. \tag{8}$$

These relations assume that we take the origin of the space-time coordinate system at the image point $\mathbf{x}$. Equations 7 and 8 represent P and S plane wave-fronts and they intersect at the image point $\mathbf{x}$. This is not a restrictive assumption, but simply indicates that we use relative space-time coordinates. The extended imaging condition shifts the source and receiver planes in space by the space-lag $\boldsymbol{\lambda}$ in the positive and negative directions, respectively, and in time by τ_p and τ_s, respectively:

$$\mathbf{p}_p \cdot (\mathbf{x} - \boldsymbol{\lambda}) \;=\; -\tau_p\,, \tag{9}$$

$$\mathbf{p}_s \cdot (\mathbf{x} + \boldsymbol{\lambda}) \;=\; +\tau_s\,. \tag{10}$$

Combining equations 7 to 10 leads to the equations:

$$\mathbf{p}_p \cdot \boldsymbol{\lambda} \;=\; \tau_p\,, \tag{11}$$

$$\mathbf{p}_s \cdot \boldsymbol{\lambda} \;=\; \tau_s\,. \tag{12}$$

Since the source and receiver wavefields have a time separation 2τ (the total time shift in equation 1), we have $\tau_p + \tau_s =$

2τ. Summing the expressions 11 and 12, we obtain:

$$(\mathbf{p}_p + \mathbf{p}_s) \cdot \boldsymbol{\lambda} = 2\tau \,. \tag{13}$$

We can also express the vectors $\mathbf{p}_p$ and $\mathbf{p}_s$ using the geometric relations between the vectors $\mathbf{n}$ and $\mathbf{q}$ and angles θ_p and θ_s as:

$$\mathbf{p}_p = \frac{\sin\theta_p}{v_p}\mathbf{q} - \frac{\cos\theta_p}{v_p}\mathbf{n} \,, \tag{14}$$

$$\mathbf{p}_s = \frac{\sin\theta_s}{v_s}\mathbf{q} + \frac{\cos\theta_s}{v_s}\mathbf{n} \,. \tag{15}$$

These two equations relate the source and receiver ray vectors with the reflector orientation and incidence/reflection angles. Substitution of $v_p = v$ and $v_s = v/\gamma$, together with the Snell's law from equation 4, into equations 14 and 15 yields

$$\mathbf{p}_p + \mathbf{p}_s = 2\frac{\sin\theta}{v}\,\mathbf{q} + \frac{\left[\sqrt{\gamma^2 - \sin^2\theta} - \cos\theta\right]}{v}\,\mathbf{n} \,, \tag{16}$$

where the angle θ denotes the incidence angle θ_p, and the variable γ is the ratio between the P- and S-wave velocities. Substituting expression 16 into equation 13, we obtain the moveout equation for PS reflections at an incidence angle θ:

$$\sin\theta\,(\mathbf{q}\cdot\boldsymbol{\lambda}) + \frac{1}{2}\left[\sqrt{\gamma^2 - \sin^2\theta} - \cos\theta\right](\mathbf{n}\cdot\boldsymbol{\lambda}) = v\tau \,, \tag{17}$$

where v and θ are the P-wave velocity and incidence angle, respectively.

For the special case of PP reflections, where $\gamma = 1$, equation 17 reduces to

$$\sin\theta\,(\mathbf{q}\cdot\boldsymbol{\lambda}) = v\tau \,, \tag{18}$$

which is the relation described by Sava & Vasconcelos (2010). Equation 17 describes the moveout function characterizing a reflection from a single shot-receiver pair. The function represents a plane in the $\{\boldsymbol{\lambda}, \tau\}$ space which depends on the incidence angle, the P-wave velocity, the V_P/V_S ratio, and the reflector defined by the vectors $\mathbf{q}$ and $\mathbf{n}$.

To confirm the validity of equation 17, we overlay this function on a CIP reflection shown in Figure 3 for a horizontal reflector (Figure 2) and in Figure 5 for a dipping reflector (Figure 4). In Figures 2 and 4, the dots on the surface at $x = 3.1$ km represent the sources and the lines on the surface represent the receivers. The dots on the reflectors indicate the CIP locations. For both experiments, panels (a) and (b) show the PP and PS reflections as a function of $\boldsymbol{\lambda}$ and τ, respectively. The lines overlaid on top of these subplots indicate that equation 17 accurately predicts the CIP moveout.

3. 2 CIP moveout for imaging with multiple shots

The CIP moveout for multiple shots can be analyzed as the stack of single-shot CIPs constructed for different angles of incidence. In the following, we define a new variable $\lambda_\tau = v\tau$ to ensure that all axes have the same dimensionality, i.e. space. Thus, the moveout function for a single shot can also be written as

$$\sin\theta\,(\mathbf{q}\cdot\boldsymbol{\lambda}) + \frac{1}{2}\left[\sqrt{\gamma^2 - \sin^2\theta} - \cos\theta\right](\mathbf{n}\cdot\boldsymbol{\lambda}) = \lambda_\tau \,. \tag{19}$$

In the following, we consider the reflection geometries in the reflection plane, thus setting the y component of all vectors to zero. Since the vector $\mathbf{q}$ at the intersection of the reflection plane and the reflector and the reflector normal vector $\mathbf{n}$ are orthogonal, we can write $\mathbf{q} = \{q_x, q_z\}$ and $\mathbf{n} = \{-q_z, q_x\}$. With the substitution of the $\mathbf{q}$ and $\mathbf{n}$ components into equation 19, we can write

$$(Aq_x - Bq_z)\,\lambda_x + (Aq_z + Bq_x)\,\lambda_z - \lambda_\tau = 0 \,, \tag{20}$$

where

$$A = \sin\theta \tag{21}$$

and

$$B = \frac{1}{2}\left[\sqrt{\gamma^2 - \sin^2\theta} - \cos\theta\right] \,. \tag{22}$$

Equation 20 states that the CIP moveout for a single shot is represented by a plane that passes through the origin of the lag space $\{\boldsymbol{\lambda}, \tau\}$ and is characterized by the vector normal $\mathbf{v} = \{Aq_x - Bq_z, Aq_z + Bq_x, -1\}$. When we consider multiple shots, the CIP moveout can be measured on the superposition of all single-shot CIP reflection planes for various angles of incidence θ. Let us consider reflections from two nearby shots whose vector normals are $\mathbf{v}_1$ and $\mathbf{v}_2$, respectively. When the incidence angle changes from θ to $\theta + d\theta$, the two CIP reflection planes from neighbouring shots intersect along a line. The cross product of the two vector normals $\mathbf{v}_1$ and $\mathbf{v}_2$ gives a vector $\mathbf{V}$, which is parallel to the intersection line. Since both planes pass through the origin, the intersection line also passes through the origin. Thus, we can simply use the vector $\mathbf{V}$ originating at the origin to represent the intersection line of two neighbouring CIP reflection planes. The moveout surface for a CIP gather is the ensemble of the intersection lines for all possible incidence angles.

To derive the intersection line formula for two adjacent CIP reflection planes, we begin by explicitly writing the vector normals of the planes from two neighbouring shots:

$$\mathbf{v}_1 = \begin{pmatrix} A_1 q_x - B_1 q_z \\ A_1 q_z + B_1 q_x \\ -1 \end{pmatrix} \,, \tag{23}$$

$$\mathbf{v}_2 = \begin{pmatrix} A_2 q_x - B_2 q_z \\ A_2 q_z + B_2 q_x \\ -1 \end{pmatrix} \,, \tag{24}$$

where

$$A_1 = \sin(\theta) \,, \tag{25}$$

$$A_2 = \sin(\theta + d\theta) \,, \tag{26}$$

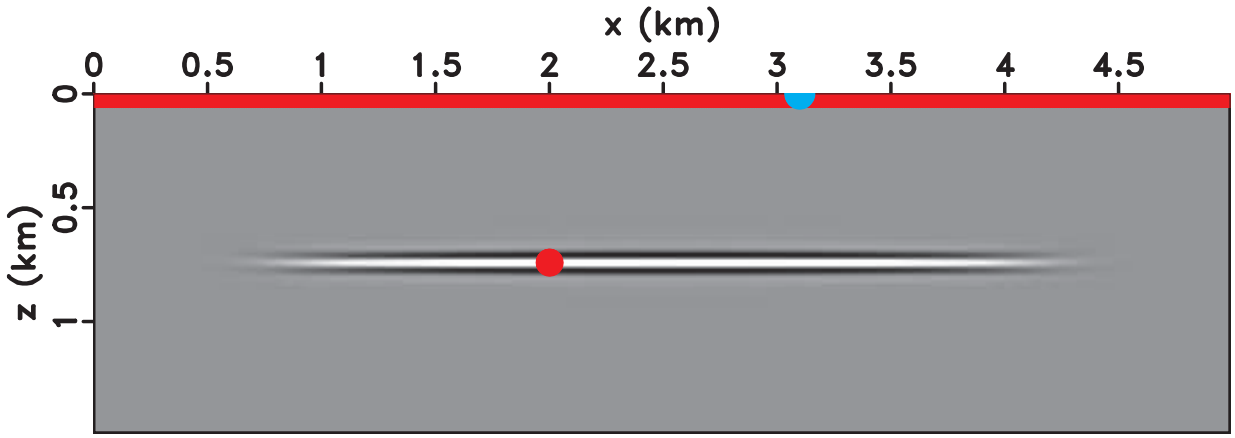


Figure 2. The experiment geometry used to construct the CIP gathers in Figure 3. The dot on the surface represents the shot location, the line on the surface represents the receivers, and the dot on the reflector represents the CIP location.

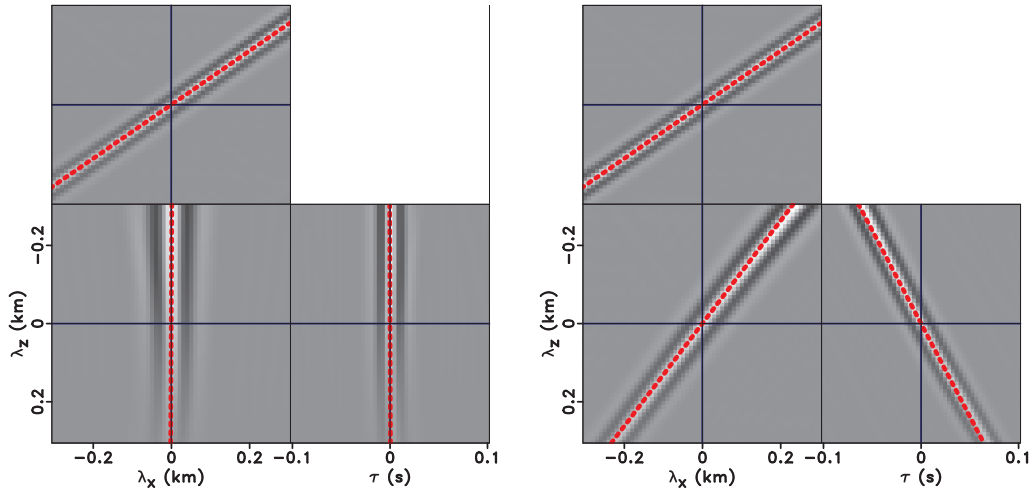


Figure 3. A common image point reflection for (a) PP data and (b) PS data for the experiment shown in Figure 2. The overlain dashed line is given by equation 17 and matches exactly with the CIP reflection moveout.

and

$$B_1 = \frac{1}{2}\left[\sqrt{\gamma^2-\sin^2\theta}-\cos\theta\right], \quad (27)$$

$$B_2 = \frac{1}{2}\left[\sqrt{\gamma^2-\sin^2(\theta+d\theta)}-\cos(\theta+d\theta)\right] \quad (28)$$

For a reflector with a dip angle α, the reflector vector $\mathbf{q}$ has components $q_x = \cos\alpha$ and $q_z = -\sin\alpha$. The intersection line, i.e. the cross product of $\mathbf{v}_1$ and $\mathbf{v}_2$, is

$$\mathbf{V} = \begin{pmatrix}\lambda_x\\ \lambda_z\\ \lambda_\tau\end{pmatrix} = d\theta\cos\theta\begin{pmatrix}\frac{1}{2}\tan\theta(1-\frac{\cos\theta}{\sqrt{\gamma^2-\sin^2\theta}})\cos\alpha+\sin\alpha\\ \frac{1}{2}\tan\theta(1-\frac{\cos\theta}{\sqrt{\gamma^2-\sin^2\theta}})\sin\alpha-\cos\alpha\\ \frac{1}{2\cos\theta}(1-\frac{\gamma^2\cos\theta}{\sqrt{\gamma^2-\sin^2\theta}})\end{pmatrix}. \quad (29)$$

By neglecting the quadratic terms $(d\theta)^2$ in the cross product of $\mathbf{v}_1$ and $\mathbf{v}_2$, we assume that the increment of the incidence angle for two nearby shots is small.

By scaling the vector $\mathbf{V}$ by an arbitrary quantity r, we

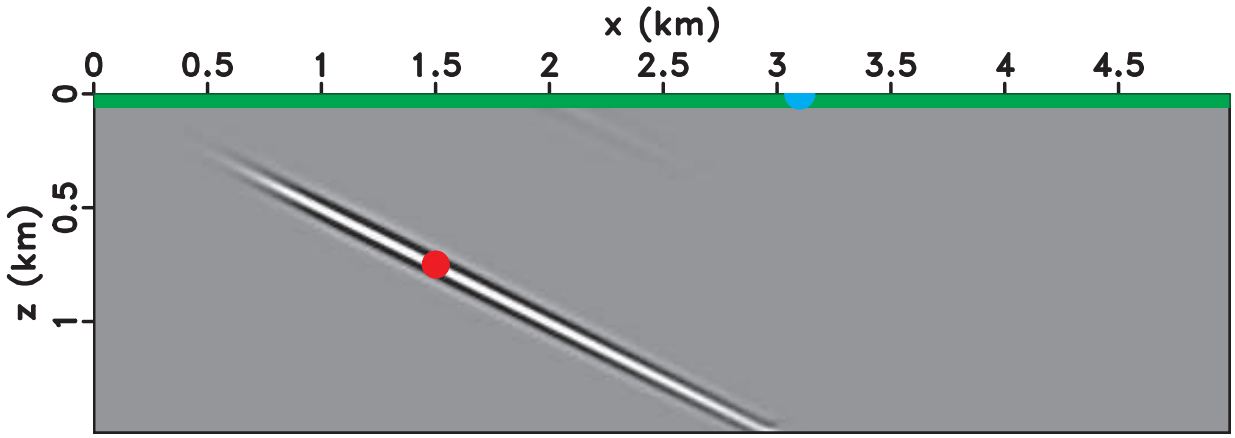


Figure 4. The experiment geometry used to construct the CIP gathers in Figure 5. The dot on the surface represents the shot location, the line on the surface represents the receivers, and the dot on the reflector represents the CIP location.

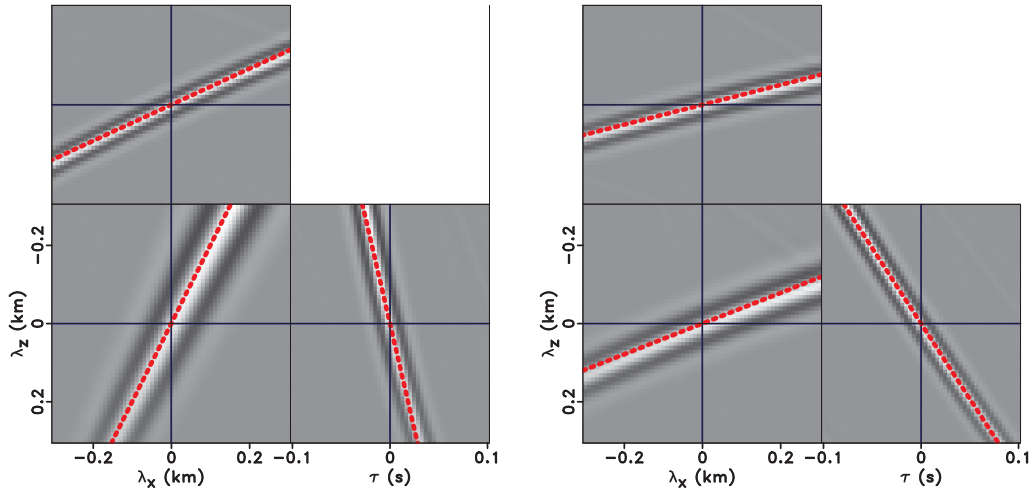


Figure 5. A common image point reflection for (a) PP data and (b) PS data for the experiment shown in Figure 4. The overlain dashed line is given by equation 17 and matches exactly with the CIP reflection moveout.

obtain the parametric form of the PS CIP surface

$$\begin{aligned} & CIP_{PS}(r,\theta,\alpha,\gamma) \\ = \; & r \begin{pmatrix} \frac{1}{2}\tan\theta(1-\frac{\cos\theta}{\sqrt{\gamma^2-\sin^2\theta}})\cos\alpha+\sin\alpha \\ \frac{1}{2}\tan\theta(1-\frac{\cos\theta}{\sqrt{\gamma^2-\sin^2\theta}})\sin\alpha-\cos\alpha \\ \frac{1}{2\cos\theta}(1-\frac{\gamma^2\cos\theta}{\sqrt{\gamma^2-\sin^2\theta}}) \end{pmatrix}, \end{aligned} \tag{30}$$

where r can take positive and negative values. The surface reduces to the simple form

$$CIP_{PP}(r,\theta,\alpha,\gamma=1) = r \begin{pmatrix} \sin\alpha \\ -\cos\alpha \\ 0 \end{pmatrix} \tag{31}$$

for pure-mode waves.

For a horizontal reflector, the CIP surface simplifies to

$$\begin{aligned} & CIP_{PS}(R,\theta,\alpha=0,\gamma) \\ = \; & r \begin{pmatrix} \frac{1}{2}\tan\theta(1-\frac{\cos\theta}{\sqrt{\gamma^2-\sin^2\theta}}) \\ -1 \\ \frac{1}{2\cos\theta}(1-\frac{\gamma^2\cos\theta}{\sqrt{\gamma^2-\sin^2\theta}}) \end{pmatrix}, \end{aligned} \tag{32}$$

by setting the reflector dip α to zero. The surface reduces to the simple form

$$CIP_{PP}(r,\theta,\alpha=0,\gamma=1) = r \begin{pmatrix} 0 \\ -1 \\ 0 \end{pmatrix} \tag{33}$$

for pure-mode waves.

We see that the CIP surfaces for a non-zero dip reflector

and for a zero-dip reflector are related by a rotation with angle α:

$$\begin{aligned} &CIP_{PS}(r,\theta,\alpha,\gamma) \\ &= \begin{pmatrix} \cos\alpha & -\sin\alpha & 0 \\ \sin\alpha & \cos\alpha & 0 \\ 0 & 0 & 1 \end{pmatrix} CIP_{PS}(r,\theta,\alpha=0,\gamma). \end{aligned} \tag{34}$$

Therefore, the CIP surface for a dipping reflector is simply a rotation about the τ axis from CIP surface for a horizontal reflector. This conclusion is valid for both PP and PS reflections. As will be discussed later, the CIP moveout equations for correct migration velocities allow us to formulate penalty functions for migration velocity analysis.

Figure 6 shows PP and PS reflections CIPs for a horizontal reflector. We plot the CIP reflection planes for all possible incidence angles and construct the intersections of these planes. In Figures 6(c) and (d), we plot the CIP line and surface for PP and PS reflections given by equations 33 and 32, respectively. The PS CIP is a smooth surface symmetric about the $\lambda_x = 0$ plane and reduces to a line along the λ_z axis for pure-mode reflections.

4 CIG AND CIP EXAMPLES

We demonstrate the CIGs and CIPs using two models: one with a horizontal reflector and the other with a dipping reflector. The moveout of the common image gathers and common image point gathers, and especially the difference of the gathers obtained with correct and incorrect velocities, give us clues about how to formulate penalty functions for migration velocity analysis. We discuss this topic in a following section.

4. 1 Horizontal reflector

In this example, we use a model with a single horizontal reflector to show the migrated images (Figure 7), space-lag domain CIGs (Figure 8), angle-domain CIGs (Figure 9), and common-image-point gathers (Figure 10), for PP and PS waves. All the images and CIGs are migrated with low, correct, and high velocities. The PS images and gathers are obtained using correct P-wave velocities, but correct or incorrect S-wave velocities. The correct P- and S-wave velocities are 3 km/s and 1.5 km/s, respectively. The low and high P-wave velocities are 2.7 km/s and 3.3 km/s, respectively, and the low and high S-wave velocities are 1.1 km/s and 1.9 km/s, respectively.

The space-lag CIGs displayed in Figure 8 are located at horizontal position $x = 2.5$ km of the model. The gathers for PP waves are all symmetric because of the lateral homogeneity of the P-wave velocity and the symmetric illumination from both sides of the CIG. The gathers for PS waves are anti-symmetric because of the polarity flip in the PS data. Compared to their PP gather counterparts, PS gathers migrated with incorrect velocities have larger curvature, i.e., they cover a smaller range of space lag λ_x in the CIGs. The radius of the CIG moveout can be predicted by the equation $R = \frac{(1-\rho^2)d}{\rho\cos\alpha}$ for homogeneous models (Yang & Sava, 2008), where d is the reflector depth, α is the reflector dip, and ρ is the ratio between the migration velocity and the real velocity. Given the same migration velocity ratio ρ for PP and PS migrations, since only the S velocity is incorrect, the effective ρ for PS data takes a smaller absolute value than that for PP data. Thus, the moveout radius R for PS data is smaller than PP data and covers a the smaller range of λ_x in the CIGs.

The angle-domain CIGs migrated with correct velocities for PP data (Figure 9(b)) and PS data (Figure 9(e)) are flat and positioned at the correct depth of the reflector. When migrated with incorrect velocity, the CIGs are non-flat and at incorrect depth. The PP gathers have continuous polarity, while the PS gathers have reversed polarity at normal incidence. The PS angle-domain CIGs show less moveout than their PP counterparts, resulted from the larger curvature in the lag-domain PS CIGs. This fact indicates that the velocity error observed on the PS image is smaller than that observed on the PP image, due to the fact that we have assumed correct P imaging velocity. In this experiment, although the shear-wave velocity errors reach $(1.5-1.1)/1.1 \approx 36\%$ (Figure 9(d)) or $(1.9-1.5)/1.5 \approx 23\%$ (Figure 9(f)), the shear-wave legs take a small fraction of the entire raypaths because the S-legs have small reflection angles. As expected, the CIGs are less sensitive to the shear-wave velocity error, because the P-wave velocity is assumed correct.

Figure 10 presents the common image point gathers for PP (panels (a), (b), and (c)) and PS data (panels (d), (e), and (f)). The CIP location is indicated by the dot on the reflector, shown in Figure 2. A total number of 61 shots from $x = 1$ km to $x = 4$ km are used for this experiment. For the correct migration velocities, the CIPs for both PP and PS data are correctly predicted by equation 32 in the previous section: the PP CIP is characterized by a line along the λ_z axis, and the PS CIP is characterized by a surface symmetric about the τ axis. For incorrect migration velocities, the CIPs deviate from this shape, which warrants their use for migration velocity analysis.

4. 2 Dipping reflector

In this second example, we use a model with a single dipping reflector. Figures 11, 12, 13 and 14 show PP and PS migrated images, space-lag CIGs, angle-domain CIGs, CIPs, respectively. The P- and S-velocity models are the same as for the preceding example, and all the images and CIGs are imaged with the same range of velocities as in the preceding example.

The space-lag CIGs at lateral position $x = 1.6$ km, shown in Figure 12, present similar features as the CIGs for horizontal reflector in the previous example. A major difference for the PS CIGs is that when incorrect S-wave migration velocity is used, the polarity flip does not occur at zero-lag. Instead, the location of the polarity flip is related to the dip of the model. This is because when incorrect migration velocities are used, the back propagated wavefields are not located at the correct reflector positions.

The angle-domain CIGs also show similar features as the

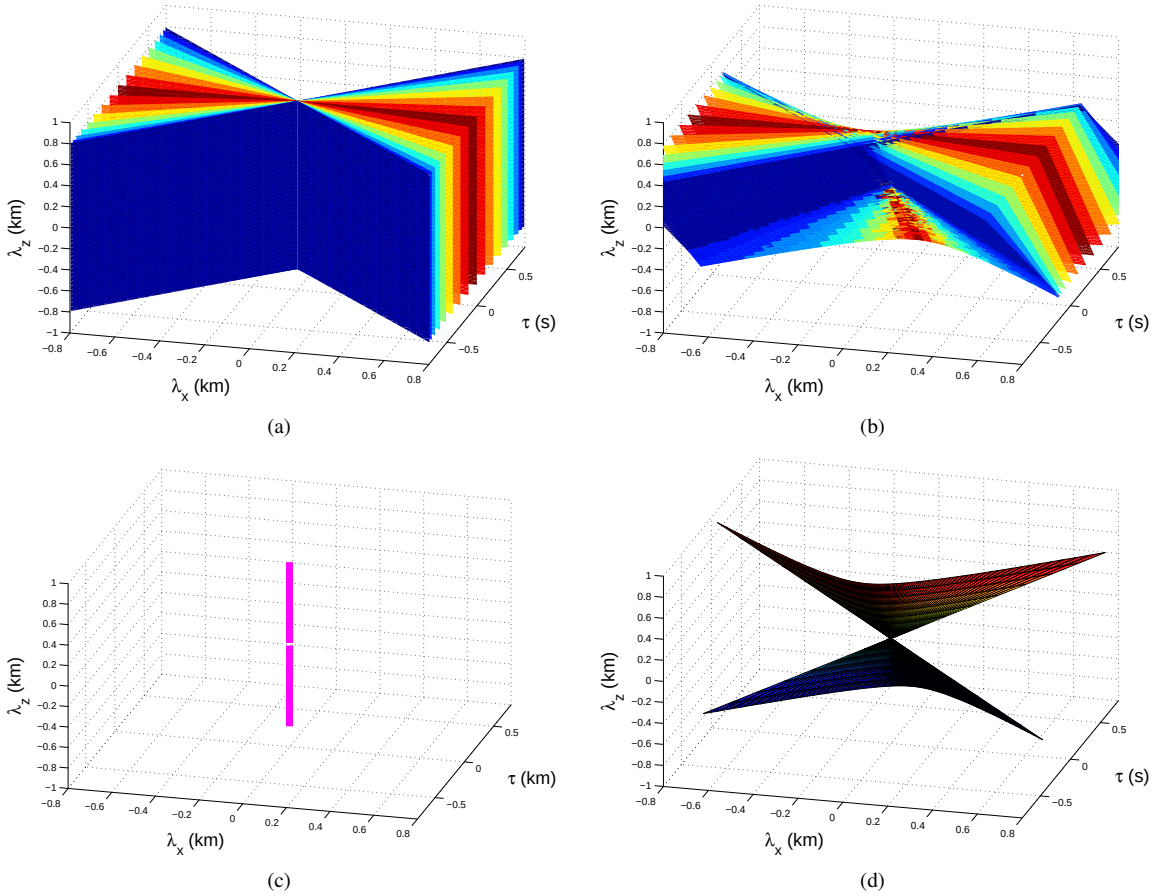


Figure 6. Common image point gather moveout for (a) PP reflection and (b) PS reflection ($\gamma = 2$). The planes in panels (a) and (b) represent reflections from individual shots. The PP reflections insect a line along λ_z axis; the PS reflections intersect a surface. Panels (c) and (d) represent the CIP line and surface predicted by the moveout equations 33 and 32, respectively.

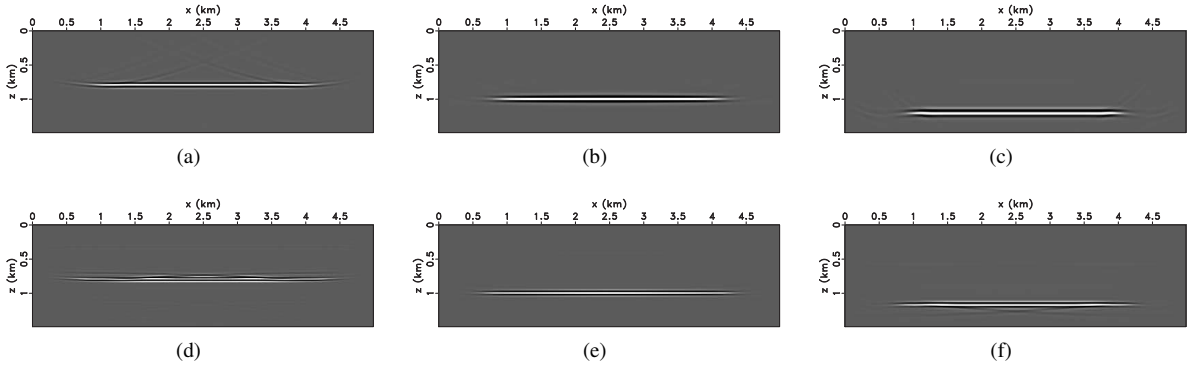


Figure 7. Migrated images for PP (upper row) and PS (lower row) data for a model with a horizontal reflector at depth $z = 1.0$ km (the same model shown in Figure 2). The images are migrated using low (left column), correct (middle column), and high (right column) velocities.

ones for horizontal reflector. When correct migration velocities are used, the gathers are flat and located at the correct reflector depth; the PP CIG has continuous polarity, and PS CIG has a polarity flip at zero incidence angle. When incorrect velocities are used for migration, the polarity flip does not occur at zero incidence angle, but at an angle related to the dip of the model. Nevertheless, the main features for the CIGs persist when correct migration velocities are used.

Figure 14 shows the CIPs for a dipping reflector. the CIP location is indicated by the dot on the reflector, shown in Fig-

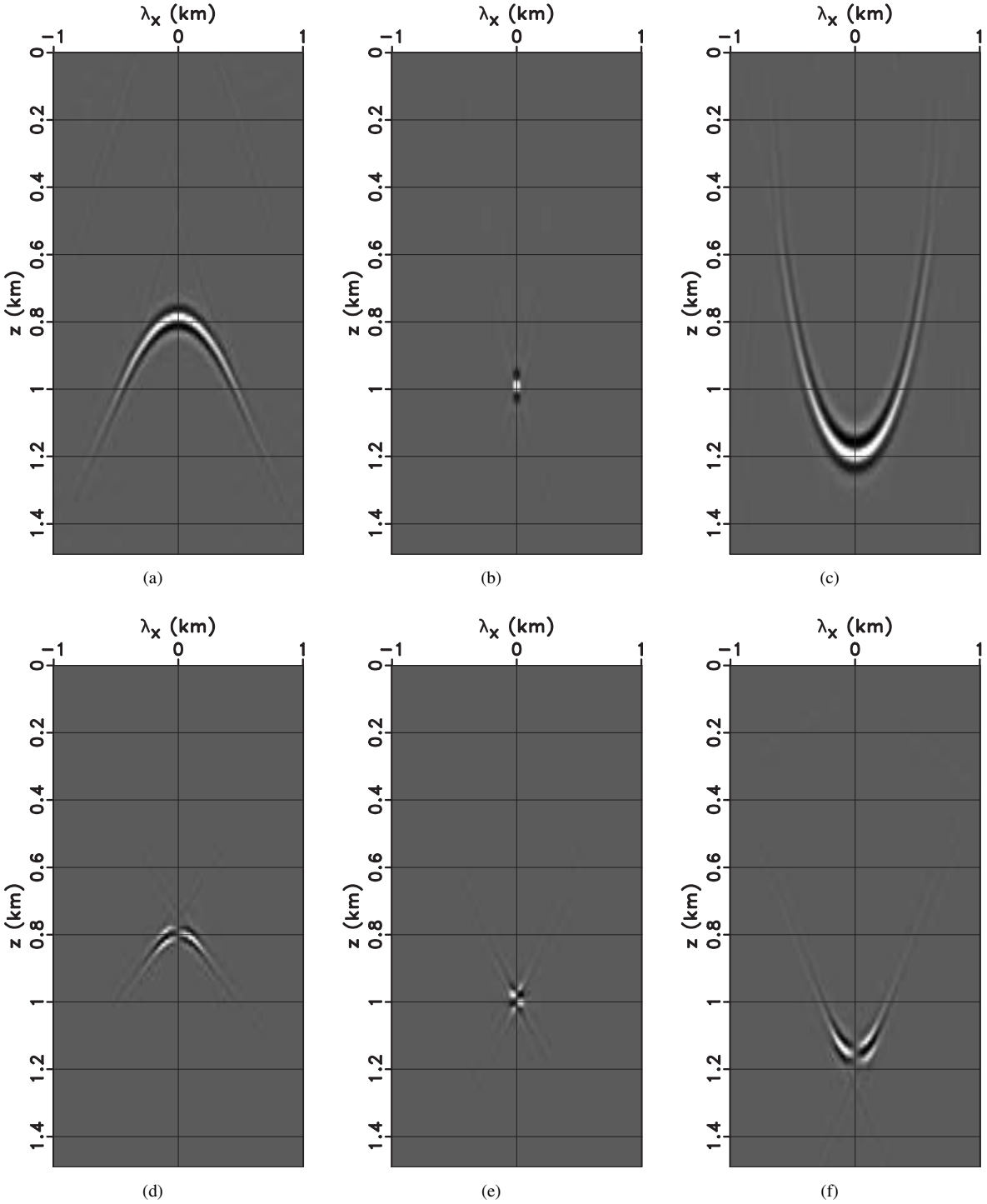


Figure 8. Space-lag CIGs for PP (upper row) and PS (lower row) data. The gathers are constructed using the extended imaging condition given by equation 2. From left to right, the gathers are constructed using low, correct, and high velocities.

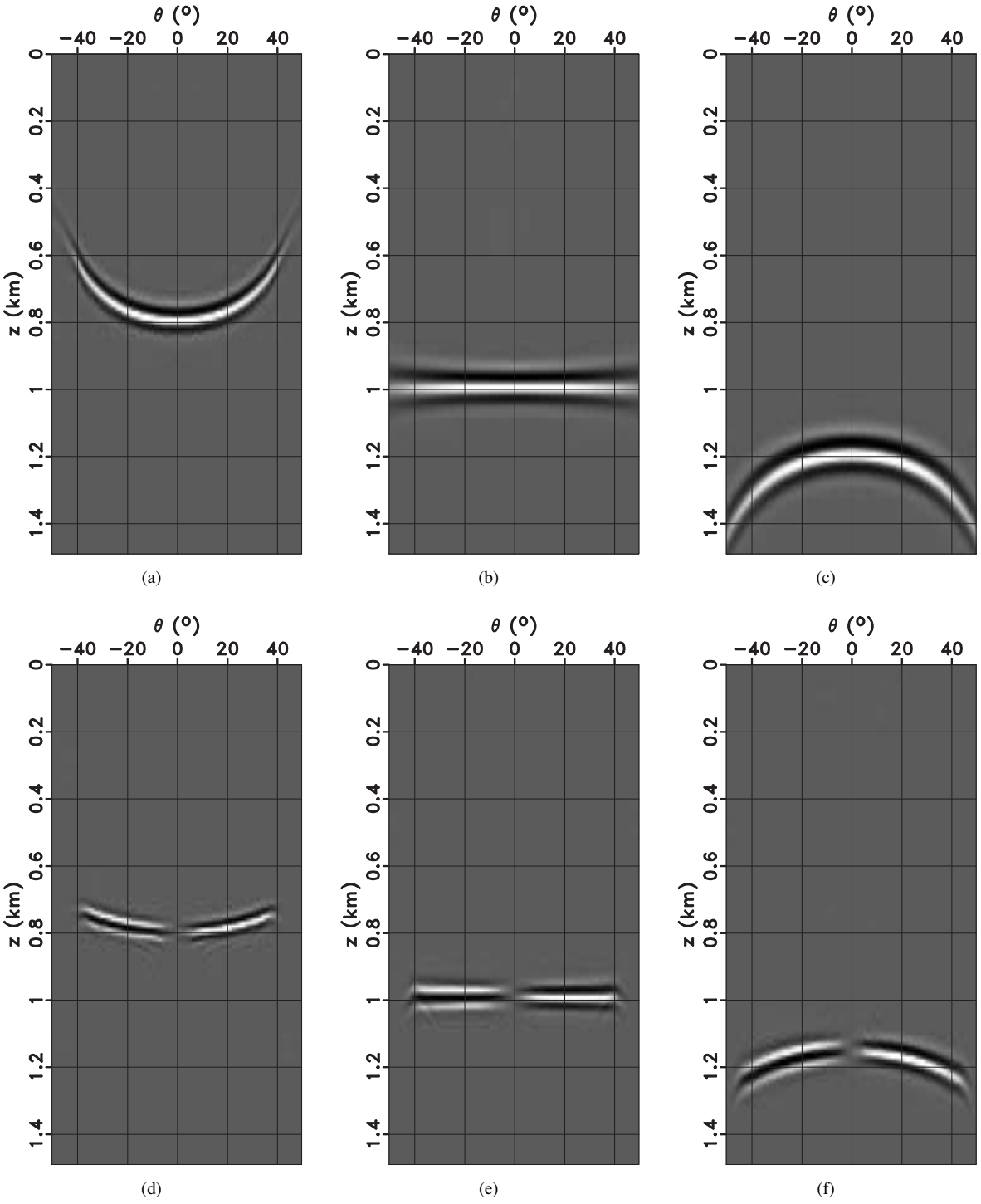


Figure 9. Angle-domain CIGs for PP (upper row) and PS (lower row) data. The gathers are mapped from the corresponding panels in Figure 8 using equation 3.

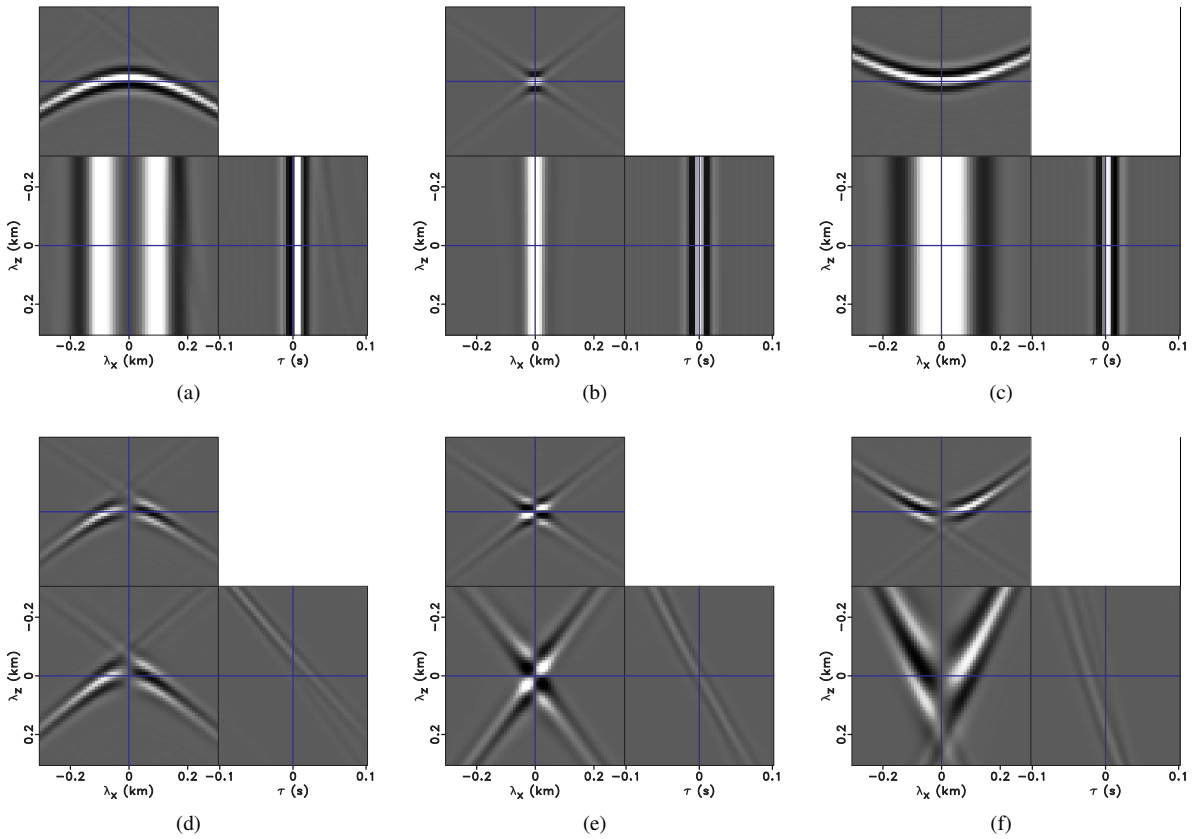


Figure 10. Common image point gathers for PP (upper row) and PS (lower row) data.The CIP location is indicated by the dot on the reflector in Figure 2. A total number of 61 shots from $x = 1$ km to $x = 4$ km are used.

ure 4. A total number of 61 shots from $x = 1$ km to $x = 4$ km are used. The PP CIP obtained with the correct migration velocity is characterized by a line oriented in a direction orthogonal to the reflector. The PS CIP obtained with the correct migration velocity is rotated from the horizontal PS CIP shown in Figure 10 by the dip angle of the reflector. This rotation indicates that the CIPs can be successfully predicted by equation 30.

5 OBJECTIVE FUNCTION FOR MIGRATION VELOCITY ANALYSIS

In order to obtain an optimized migration velocity model, an objective function that reaches its minimum at correct velocity is needed. Shen et al. (2003), Shen (2004), and Shen & Symes (2008) propose the use of differential semblance criteria to formulate the objective function. A differential semblance optimization (DSO) operator P defines a residual by penalizing the departure of image gathers from an ideal shape corresponding to the image constructed with correct velocity. The application of an operator P to the gathers $R(\mathbf{x}, \boldsymbol{\lambda})$ or $R(\mathbf{x}, \theta)$ at incorrect velocity gives an image residual. Thus, the optimization problem can be formulated by minimizing the objective function:

$$J = \frac{1}{2}\|P[R]\|\,. \tag{35}$$

The objective function for wave-equation migration velocity analysis can be defined using images constructed as a function of cross-correlation lags (Rickett & Sava, 2001) or reflection angles (Sava & Fomel, 2003). In particular, we can select subsets of extended images CIGs or CIPs to perform migration velocity analysis.

5. 1 PP and PS penalty function for common image gathers

The DSO operators for CIGs in the space-lag domain is give by (Shen, 2004):

$$P_{\boldsymbol{\lambda}}[R] = |\boldsymbol{\lambda}|\, R\,. \tag{36}$$

Based on the fact that the lag- and angle-domain gathers are related by a Radon transform, Shen (2004) shows the equivalence of using the DSO operator in equation 36 for space-lag gathers with a more conventional derivative applied to angle-domain CIGs.

For CIGs at correct migration velocities, the difference

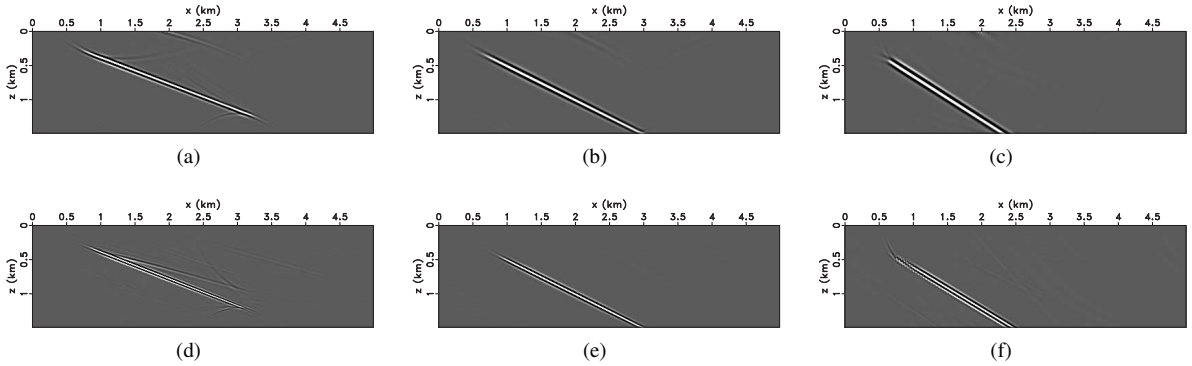


Figure 11. Migrated images for PP (upper row) and PS (lower row) data for a model with a 22° dipping reflector (the same model shown in Figure 4). The images are migrated using low (left column), correct (middle column), and high (right column) velocities.

between PP and PS angle domain CIG is that$R_{PP} = R(\mathbf{x}, \theta)$ is an even function of θ, while $R_{PS} = R(\mathbf{x}, \theta)$ is an odd function of θ. Since, the PP and PS angle-domain CIGs are both flat when migration velocities are correct, we conjecture that it is valid to use the same penalty operator for PP and PS gathers. This penalty function only kinematically penalizes the moveout, and therefore amplitude variation versus angles of the events in the angle gathers does not influence our choice of penalty functions.

It can be expected that because the PS gathers (in both lag- and angle-domains) are constructed with velocity errors only in the receiver wavefield, the objective functions for PS gathers are flatter than those for the PP gathers. This is illustrated in Figure 15, which shows the objective function $J = \frac{1}{2}\|P_{\boldsymbol{\lambda}}[R]\|$ for the PP and PS images constructed for the model shown in Figure 7, migrated with velocities scaled by constant values with respect to the correct velocity. For PS migration, the P velocity is assumed to be correct, and only the S-wave velocity has errors.

5. 2 PP and PS penalty function for common image point gathers

The simple form of the CIP for PP images allows for an easy formulation of a penalty function. For a horizontal reflector, the PP CIP is a line along the λ_z axis, which makes it natural to penalize the events in a CIP by the radial distance from this axis:

$$P_{(\lambda_x,\lambda_z,\lambda_\tau)}[R] = R\sqrt{\lambda_x^2 + \lambda_\tau^2}\,. \tag{37}$$

For a dipping reflector, the PP CIP is oriented at a direction perpendicular to the reflector in the $\{\boldsymbol{\lambda}, \tau\}$ space. We can formulate a penalty function by the distance from this tilted line:

$$P_{(\lambda_x,\lambda_z,\lambda_\tau)}[R] = R\sqrt{(\lambda_x \cos\alpha + \lambda_z \sin\alpha)^2 + \lambda_\tau^2}\,, \tag{38}$$

where α is the dip of the reflector at the CIP location. In a more compact form, the above equation can be written as

$$P_{(\boldsymbol{\lambda},\lambda_\tau)}[R] = R\sqrt{(\mathbf{q}\cdot\boldsymbol{\lambda})^2 + \lambda_\tau^2}\,. \tag{39}$$

Similarly, for PS gathers we can define a penalty function which increases with distance from the surface defined by equation 30 and shown in Figure 6(b). Since the PS CIP for a dipping reflector is a rotation of that for a horizontal reflector, we start our analysis from the CIP for a horizontal reflector, which has a simpler form. Figure 16 shows the geometry used for construction of penalty function for PS images. The surface characterizes the moveout in a the CIP gather for a horizontal reflector and is based on equation 32. The PS CIP surface for a horizontal reflector is symmetric about the plane $\lambda_x = 0$ and this plane intersects the CIP surface along a line L, whose form can be obtained by setting the incidence angle θ to zero in equation 32:

$$L(\gamma, \alpha = 0) = r \begin{pmatrix} 0 \\ -1 \\ \frac{1-\gamma}{2} \end{pmatrix}\,. \tag{40}$$

This line is a symmetry axis of the CIP surface. In the symmetry plane $\lambda_x = 0$, we can find a vector $\mathbf{A}$ perpendicular to this intersection line L:

$$\mathbf{A}(\gamma, \alpha = 0) = \begin{pmatrix} 0 \\ \frac{\gamma-1}{2} \\ -1 \end{pmatrix}\,, \tag{41}$$

The vector $\mathbf{A}$ is an axis used for measuring the distance from the CIP surface.

For a dipping reflector, the entire CIP surface is rotated from that of a horizontal reflector by the dip angle α. The shape of the CIP surface remains the same, which enables us to find the symmetry plane of the CIP surface by setting $\theta = 0$ in equation 30:

$$L(\gamma, \alpha) = r \begin{pmatrix} -\sin\alpha \\ -\cos\alpha \\ \frac{1-\gamma}{2} \end{pmatrix}\,, \tag{42}$$

Note that this line is rotated from the one defined by equation 40 by the dip angle α about the λ_τ axis. A vector perpendicular to this intersection line in the symmetry plane can also be obtained by rotating equation 41 by an angle α about the

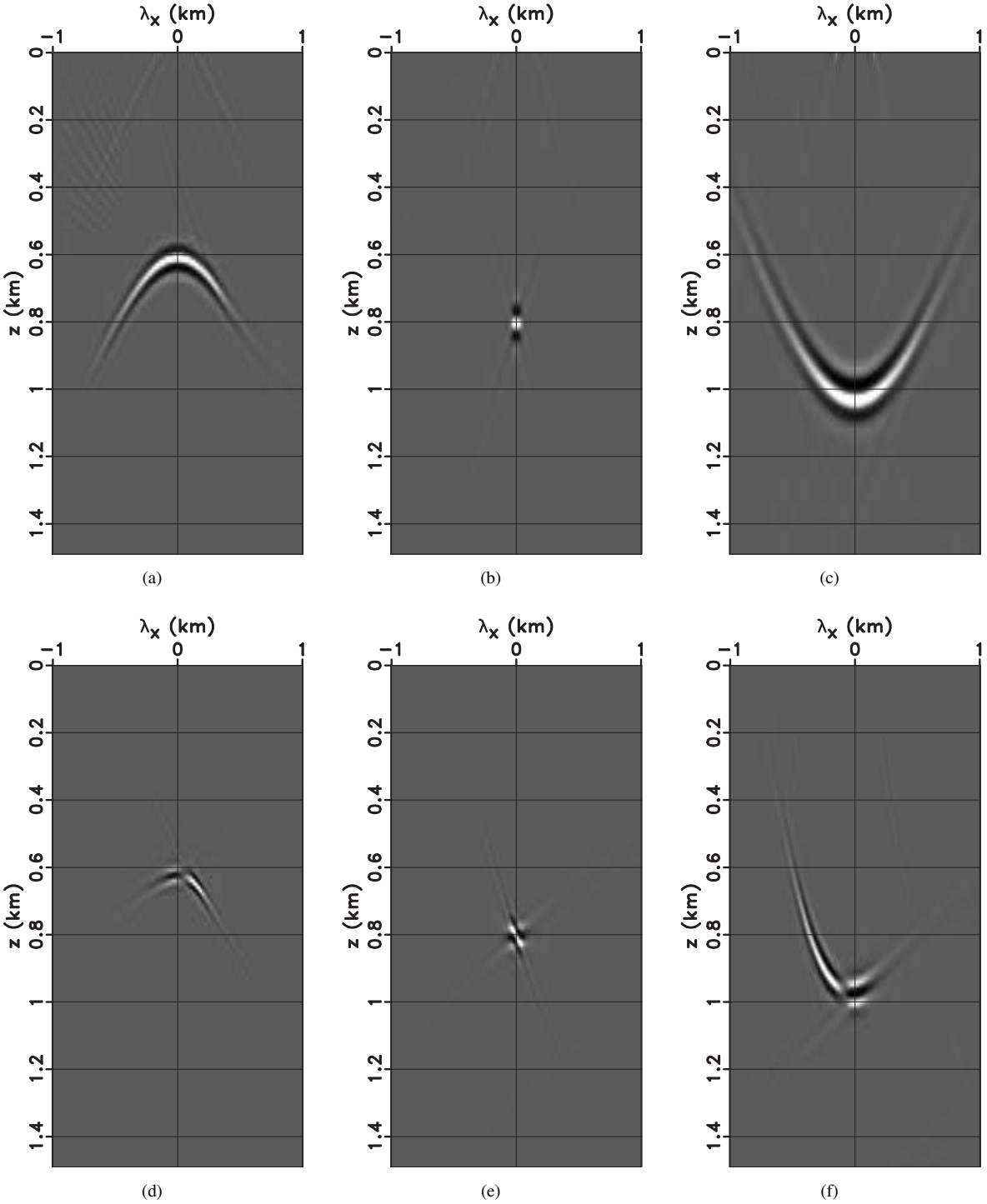


Figure 12. Space-lag CIGs for PP (upper row) and PS (lower row) data. The gathers are constructed using the extended imaging condition given by equation 2. From left to right, the gathers are constructed using low, correct, and high velocities.

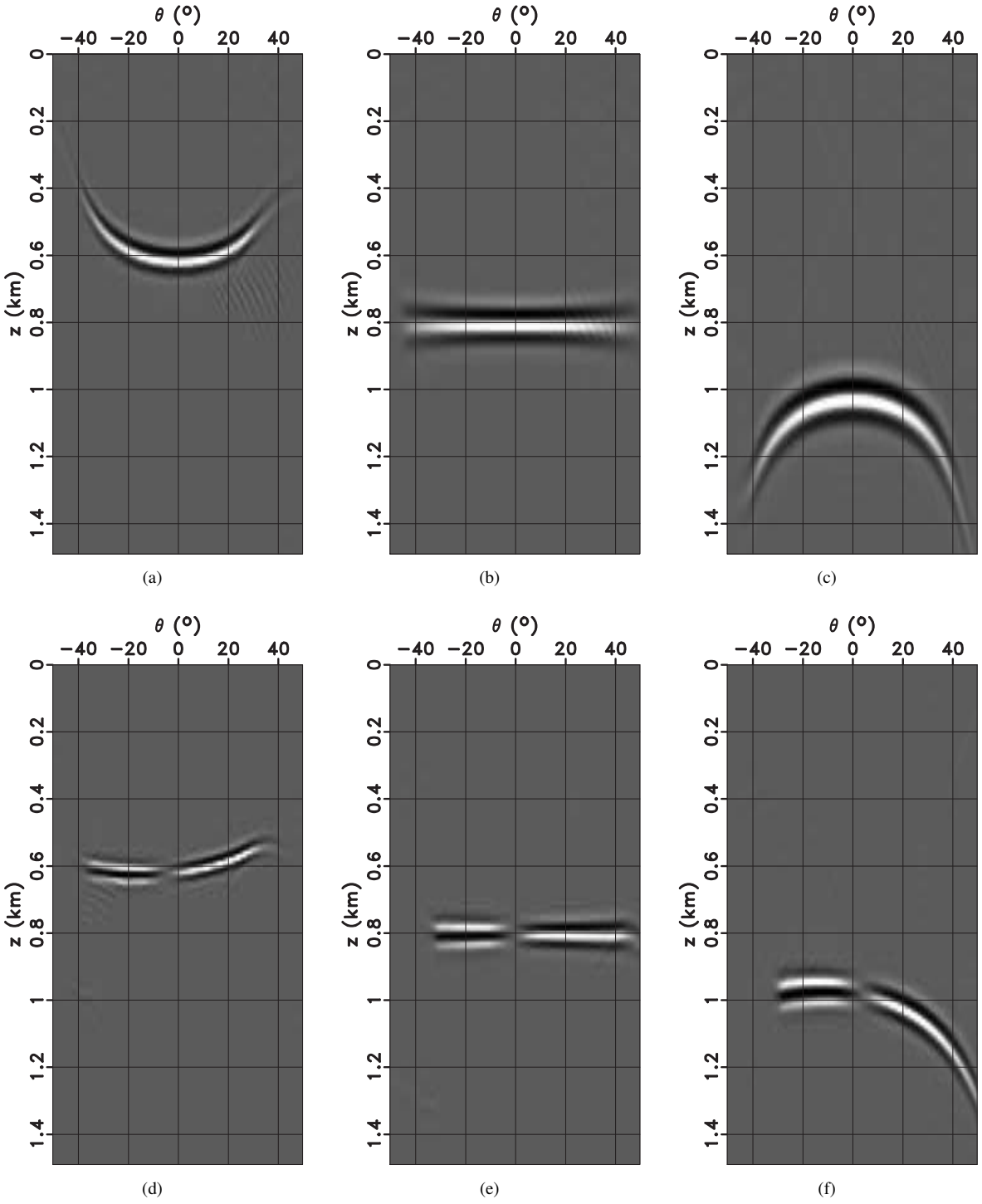


Figure 13. Angle-domain CIGs for PP (upper row) and PS (lower row) data. The gathers are mapped from corresponding panels in Figure 8 using equation 3. The dip used for the angle decomposition is obtained from the migrated images in Figure 11.

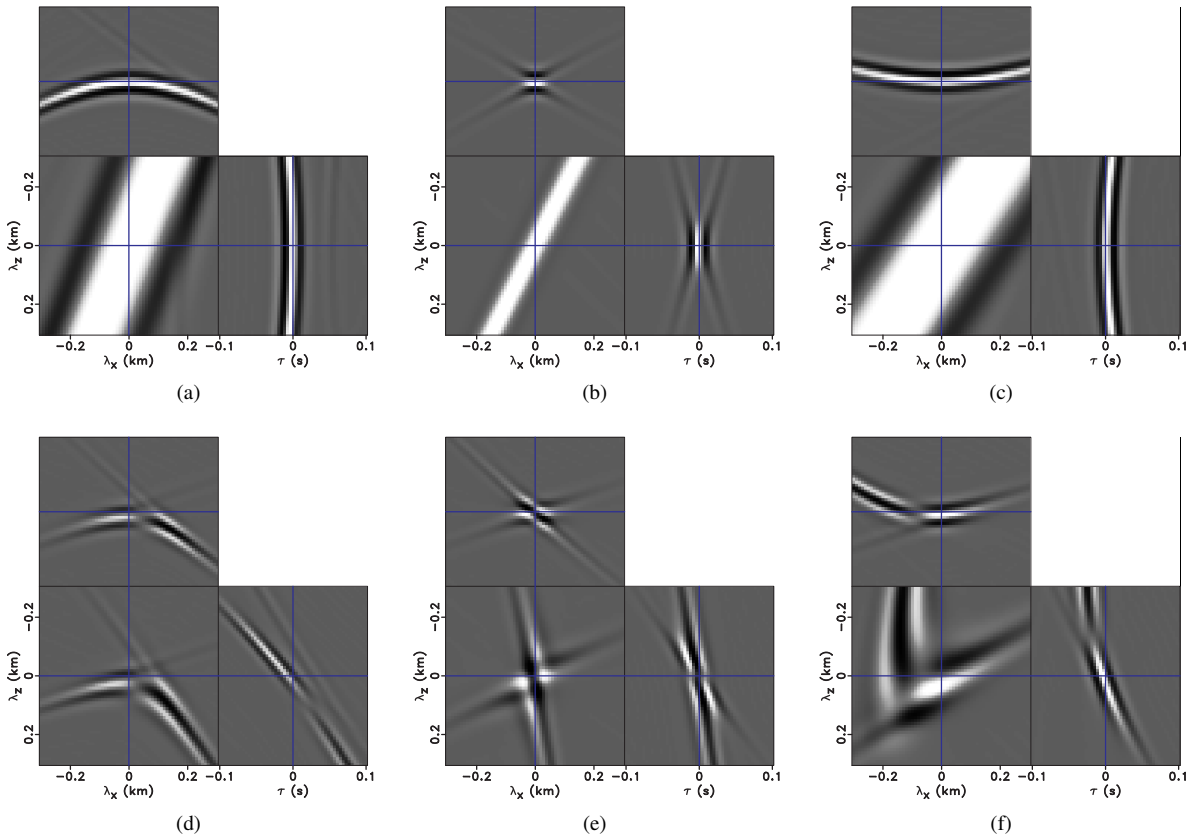


Figure 14. Common image point gathers for PP (upper row) and PS (lower row) data.The CIP location is indicated by the dot on the reflector in Figure 4. A total number of 61 shots from $x = 1$ km to $x = 4$ km are used.

λ_τ axis:

$$\mathbf{A}(\gamma,\alpha) = \begin{pmatrix} \frac{\gamma-1}{2}\sin\alpha \\ \frac{\gamma-1}{2}\cos\alpha \\ -1 \end{pmatrix} . \qquad (43)$$

The line defined by this vector reduces to the line given by equation 41 for $\alpha = 0$.

Based on the geometry shown in Figure 16, we construct a penalty function as the superposition of shifted CIP surfaces corresponding to various distances from the surface defined by equation 30. These surfaces in the $\{\boldsymbol{\lambda}, \tau\}$ space are both shifted by a distance d along the axis vector $\mathbf{A}(\gamma,\alpha)$ and also scaled by a factor d. A possible CIP penalty function is thus given by the parametric form

$$\begin{aligned} & P_{(\lambda_x,\lambda_z,\lambda_\tau,\alpha,\gamma)}[R] \\ = \; & P_{(\lambda_x(r,\theta),\lambda_z(r,\theta),\lambda_\tau(r,\theta),\alpha,\gamma)}[R] \\ = \; & R\sum_d |d| \cdot \left[CIP_{PS}(r,\theta,\alpha,\gamma) - d\frac{\mathbf{A}(\alpha)}{|\mathbf{A}(\alpha)|} \right] \end{aligned} \qquad (44)$$

Here, d ranges from negative to positive values along the axis defined by vector $\mathbf{A}(\gamma,\alpha)$.

We plot the PP (equation 37) and PS (equation 44) penalty functions in Figure 17 for both horizontal (panels (c) and (d)) and dipping (panels (c) and (d)) reflectors. The penalty function is zero at the CIP line/surface (shown in Figures 10(b) and (e) for horizontal reflectors, and in Figures 14(b) and (e) for dipping reflectors), and increases away from the line/surface. Figure 18 shows the objective function $J = \frac{1}{2}\|P_{(\boldsymbol{\lambda},\lambda_\tau)}[R]\|$ for both PP and PS data. The well behaved convex functions indicate that the formulated penalty functions can be used for migration velocity analysis.

6 CONCLUSIONS

We study the features of common image gathers and common image point gathers. For correct migration velocities, the CIGs are characterized by focused points in the lag domain and by flat events in the angle domain. For incorrect migration velocities, the CIGs are misfocusing in the lag domain and are non-flat in the angle domain. The PP CIGs show continuous polarity, while the PS CIGs have polarity reversals at zero space-lags or zero incidence angles for correct velocity, or away from these points for incorrect velocity.

For correct migration velocities, the CIPs for pure wave-modes are characterized by a line in the space- and time-lag space oriented orthogonal to the reflector; the CIPs for converted-waves are characterized by surfaces which contain

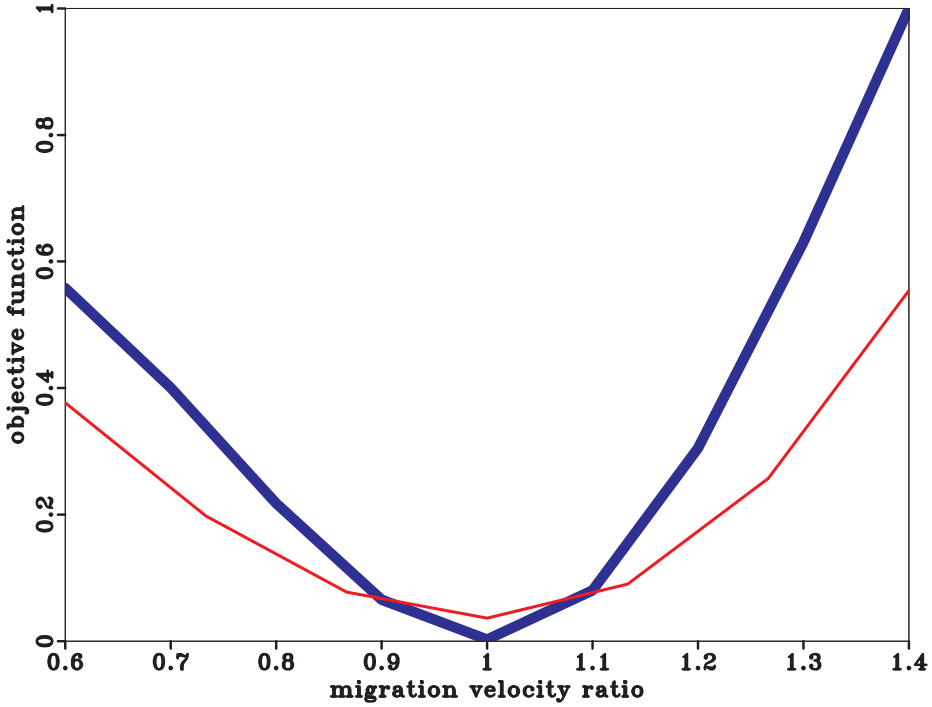


Figure 15. Objective function for PP and PS CIPs by applying the penalty functions $P_{\boldsymbol{\lambda}} = |\boldsymbol{\lambda}|$ to PP and PS CIGs, respectively. The thick line is the curve for PP data, and the thin line is the curve for PS data. The horizontal axis is the ratio of migration velocity and true model velocity. The PS CIP gathers are obtained using correct P-wave velocity.

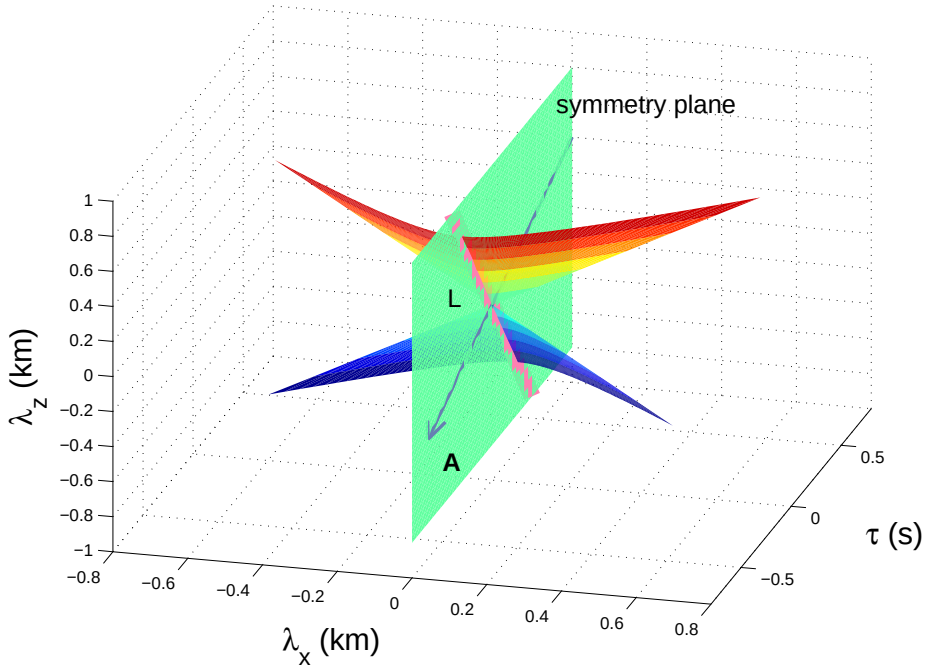


Figure 16. A cartoon showing the penalty function construction for PS CIPs. For simplicity, we use a horizontal reflector in this cartoon. The curved surface is the CIP surface for PS data, and the plane $\lambda_x = 0$ is the symmetry axis of the surface. The CIP surface and its symmetry axis intersect along the line L. In the symmetry plane, we can find a vector $\mathbf{A}$ perpendicular to the line L.

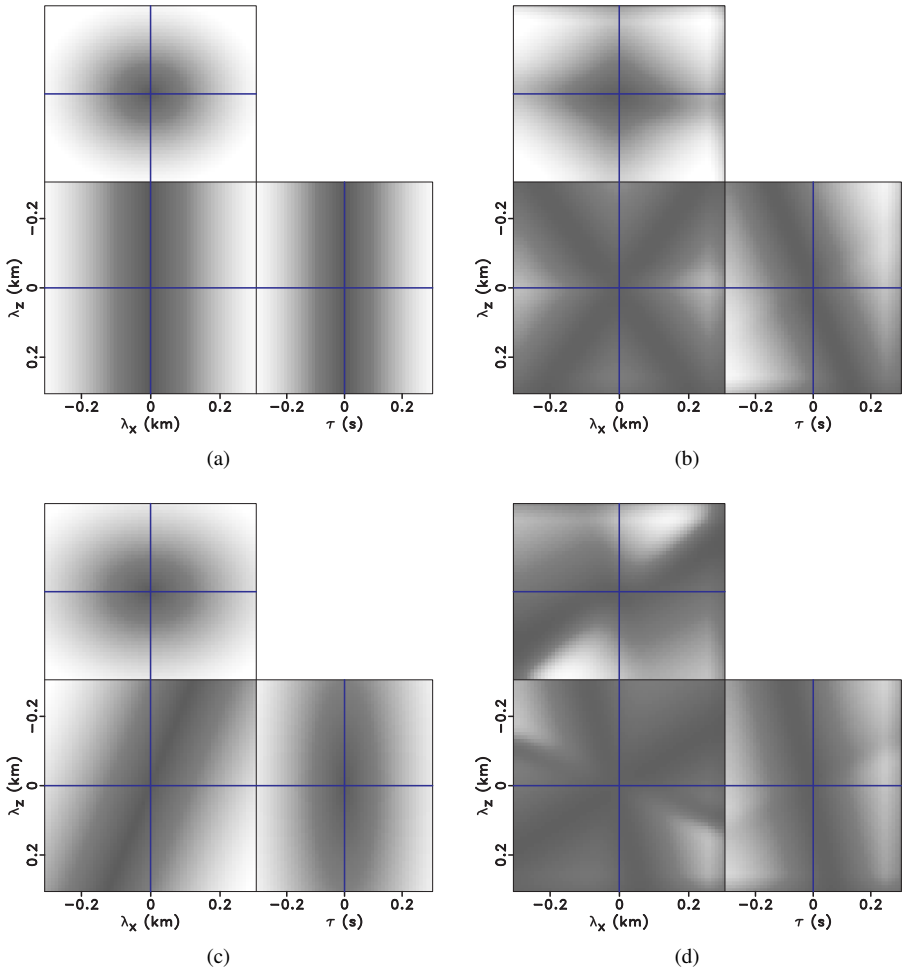


Figure 17. Panels (a) to (d) show penalty functions for PP horizontal, PS horizontal, PP dipping, PS dipping CIPs, respectively. The PP and PS penalty functions are given byequations 39 and 44, respectively. The dips used for panels (c) and (d) are both 22 °.

the origin of the space- and time-lag space. For incorrect migration velocities, the PP CIPs are not characterized by focused lines but by surfaces which depend on the migration velocities; the PS CIPs are also characterized by surfaces deviating from their ideal shape corresponding to correct velocity.

The deviation of CIGs and CIPs gathers obtained with incorrect migration velocities from the ones obtained with correct migration velocities warrants their use for migration velocity analysis. We use differential semblance optimization (DSO) to define penalty functions for CIGs and CIPs and for PP and PS waves. We formulate objective functions by penalizing the departure of the gathers from the ideal shape obtained with correct migration velocities. The objective functions for both CIGs and CIPs and for both PP and PS data are convex, which allows their use in velocity optimization using gradient-descent methods.

7 ACKNOWLEDGMENTS

The reproducible numeric examples in this paper use the Madagascar open-source software package freely available from http://www.reproducibility.org.

REFERENCES

Albertin, U., Sava, P., Etgen, J., and Maharramov, M., 2006, Adjoint wave-equation velocity analysis: 74th Annual International Meeting, SEG, Expanded Abstracts, 3009–3013.

Biondi, B., and Sava, P., 1999, Wave-equation migration velocity analysis: SEG Technical Program Expanded Abstracts, **18**, no. 1, 1723–1726.

Dai, H., Li, X. Y., and Mueller, M., 2000, Compensating for the effects of gas clouds by prestack migration: A case study from Valhall: Compensating for the effects of gas clouds by prestack migration: A case study from Valhall:, Soc. of Expl. Geophys., 70th Ann. Internat. Mtg, 1047–1050.

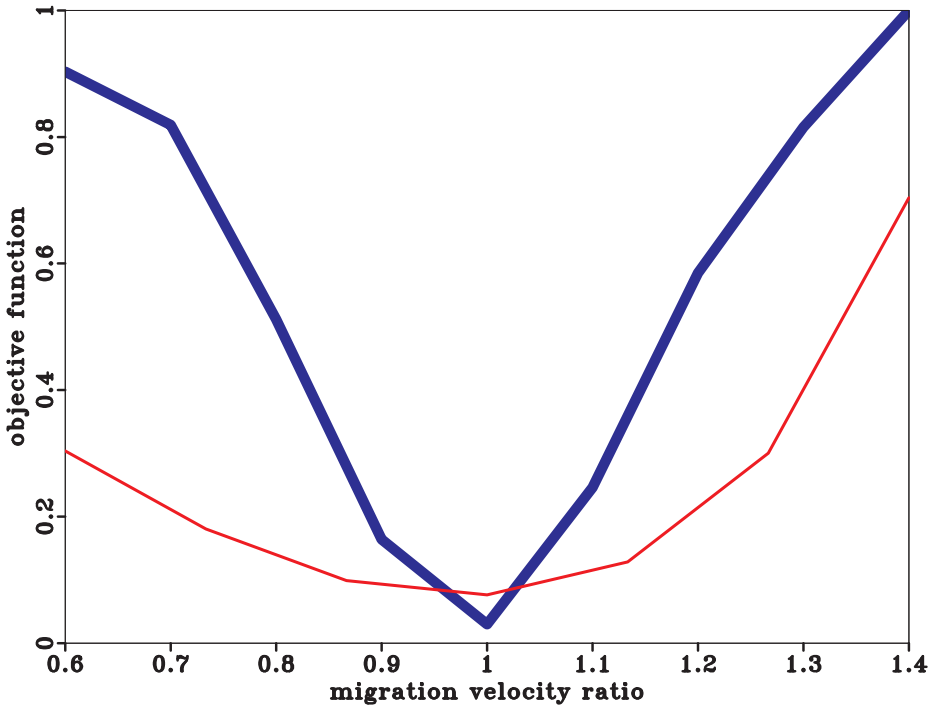


Figure 18. Objective function for PP and PS CIPs by applying the penalty functions, Figure 17(a) and (b), to PP and PS CIP gathers respectively. The thick line is the curve for PP data, and the thin line is the curve for PS data. The horizontal axis is the ratio of migration velocity and true model velocity. The PS CIP gathers are obtained using correct P-wave velocity.

Fomel, S., and Backus, M. M., 2003, Multicomponent seismic data registration by least squares: SEG Technical Program Expanded Abstracts, **22**, no. 1, 781–784.

Fomel, S., Backus, M., Fouad, K., Hardage, B., and Winters, G., 2005, A multistep approach to multicomponent seismic image registration with application to a West Texas carbonate reservoir study: SEG Technical Program Expanded Abstracts, **24**, no. 1, 1018–1021.

Gaiser, J. E., 1996, Multicomponent Vp/Vs correlation analysis: Geophysics, **61**, no. 04, 1137–1149.

Herrenschmidt, A., Granger, P.-Y., Audebert, F., Gerea, C., Etienne, G., Stopin, A., Alerini, M., Lebegat, S., Lambaré, G., Berthet, P., Nebieridze, S., and Boelle, J.-L., 2001, Comparison of different strategies for velocity model building and imaging of PP and PS real data: The Leading Edge, **20**, no. 9, 984–995.

Kendall, R. R., Gray, S. H., and Murphy, G. E., 1998, Subsalt imaging using prestack depth migration of converted waves: Mahogany Field, Gulf of Mexico: Subsalt imaging using prestack depth migration of converted waves: Mahogany Field, Gulf of Mexico:, Soc. of Expl. Geophys., 68th Ann. Internat. Mtg, 2052–2055.

Margrave, G. F., Stewart, R. R., and Larsen, J. A., 2001, Joint PP and PS seismic inversion: The Leading Edge, **20**, no. 9, 1048–1052.

Mora, P., 1988, Elastic wave-field inversion of reflection and transmission data: Geophysics, **53**, no. 06, 750–759.

Nickel, M., and Sonneland, L., 2004, Automated PS to PP event registration and estimation of a high-resolution Vp-Vs ratio volume: Automated PS to PP event registration and estimation of a high-resolution Vp-Vs ratio volume:, Soc. of Expl. Geophys., 74th Ann. Internat. Mtg., 869–872.

Nicoletis, L. M., Svay-Lucas, J., and Prigent, H., 1998, True amplitude pre-stack imaging of converted waves: True amplitude pre-stack imaging of converted waves:, Soc. of Expl. Geophys., 68th Ann. Internat. Mtg, 734–737.

Ogiesoba, O. C., and Stewart, R. R., 2003, Vp/Vs from multicomponent seismic data and automatic PS to PP time mapping: SEG Technical Program Expanded Abstracts, **22**, no. 1, 789–792.

Pratt, R. G., and Worthington, M. H., 1990, Inverse theory applied to multi-source cross-hole tomography. part 1: Acoustic wave-equation method: Geophys. Prosp., **38**, no. 03, 287–310.

Pratt, R. G., 1999, Seismic waveform inversion in the frequency domain, Part 1: Theory and verification in a physical scale model: Geophysics, **64**, no. 3, 888–901.

Rickett, J., and Sava, P., 2001, Offset and angle domain common-image gathers for shot-profile migration: Offset and angle domain common-image gathers for shot-profile migration:, Soc. of Expl. Geophys., 71st Ann. Internat. Mtg, 1115–1118.

Sava, P. C., and Fomel, S., 2003, Angle-domain common-image gathers by wavefield continuation methods: Geo-

physics, **68**, no. 3, 1065–1074.

Sava, P., and Fomel, S., 2005a, Coordinate-independent angle-gathers for wave equation migration: SEG Technical Program Expanded Abstracts, **24**, no. 1, 2052–2055.

——— 2005b, Wave-equation common-angle gathers for converted waves: SEG Technical Program Expanded Abstracts, **24**, no. 1, 947–950.

Sava, P., and Fomel, S., 2006, Time-shift imaging condition in seismic migration: Geophysics, **71**, no. 6, S209–S217.

Sava, P., and Vasconcelos, I., 2010, Extended imaging condition for wave-equation migration: Geophysical Prospecting, in press.

Shen, P., and Symes, W. W., 2008, Automatic velocity analysis via shot profile migration: Geophysics, **73**, no. 5, VE49–VE59.

Shen, P., Stolk, C., and Symes, W., 2003, Automatic velocity analysis by differential semblance optimization: 73th Annual International Meeting, SEG, Expanded Abstracts, 2132–2135.

Shen, P., 2004, Wave-equation migration velocity analysis by differential semblance optimization: Ph.D. thesis, Rice Univeristy.

Song, Z. M., Williamson, P. R., and Pratt, R. G., 1995, Frequency-domain acoustic-wave modeling and inversion of crosshole data: Part II: Inversion method, synthetic experiments and real-data results: Geophysics, **60**, no. 03, 796–809.

Stewart, R. R., Gaiser, J., Brown, R. J., and Lawton, D. C., 2002, Converted-wave seismic exploration: Methods: Geophysics, **67**, no. 05, 1348–1363.

Stewart, R. R., Gaiser, J., Brown, R. J., and Lawton, D. C., 2003, Converted-wave seismic exploration: Applications: Geophysics, **68**, no. 1, 40–57.

Tarantola, A., 1987, Inverse Problem Theory: methods for data fitting and model parameter estimation: , Elsevier Science Publ. Co., Inc.

Thomsen, L., 1998, Converted-wave reflection seismology over anisotropic, inhomogenous media: Converted-wave reflection seismology over anisotropic, inhomogenous media:, Soc. of Expl. Geophys., 68th Ann. Internat. Mtg, 2048–2051.

Veire, H. H., and Landrø, M., 2006, Simultaneous inversion of PP and PS seismic data: Geophysics, **71**, no. 3, R1–R10.

Yan, J., and Sava, P., 2008, Isotropic angle-domain elastic reverse-time migration: Geophysics, **73**, no. 6, S229–S239.

Yang, T., and Sava, P., 2008, Wave-equation extended images for semblance and depth focusing velocity analysis: SEG Technical Program Expanded Abstracts, **27**, no. 1, 2351–2355.

Yang, T., and Sava, P., 2009, Wave-equation migration velocity analysis using extended images: SEG Technical Program Expanded Abstracts, **28**, no. 1, 3715–3719.

Yuan, J. J., Nathan, G., Calvert, A., and Bloor, R., 2008, Automated C-wave registration by simulated annealing: SEG Technical Program Expanded Abstracts, **27**, no. 1, 1043–1047.